energies

Article

Improved Electrical and Thermal Conductivities of Graphene–Carbon Nanotube Composite Film as an Advanced Thermal Interface Material

Youcheng Jiang [1], Shangzhi Song [2], Mengjuan Mi [1], Lixuan Yu [1], Lisha Xu [3,*], Puqing Jiang [2,*] and Yilin Wang [1,*]

[1] School of Microelectronics, Shandong Technology Center of Nanodevices and Integration, Shandong University, Jinan 250100, China
[2] School of Energy and Power Engineering, Huazhong University of Science and Technology, Wuhan 430074, China
[3] School of Physics, Hubei University, Wuhan 430062, China
* Correspondence: lisha.whu@hotmail.com (L.X.); jpq2021@hust.edu.cn (P.J.); yilinwang@email.sdu.edu.cn (Y.W.)

Abstract: Thermal management has become a crucial issue for the rapid development of electronic devices, and thermal interface materials (TIMs) play an important role in improving heat dissipation. Recently, carbon−based TIMs, including graphene, reduced graphene oxide, and carbon nanotubes (CNTs) with high thermal conductivity, have attracted great attention. In this work, we provide graphene−carbon nanotube composite films with improved electrical and thermal conductivities. The composite films were prepared from mixed graphene oxide (GO) and CNT solutions and then were thermally reduced at a temperature greater than 2000 K to form a reduced graphene oxide (rGO)/CNT composite film. The added CNTs connect adjacent graphene layers, increase the interlayer interaction, and block the interlayer slipping of graphene layers, thereby improving the electrical conductivity, through−plane thermal conductivity, and mechanical properties of the rGO/CNT composite film at an appropriate CNT concentration. The rGO/CNT(4:1) composite film has the most desired properties with an electrical conductivity of ~2827 S/cm and an in−plane thermal conductivity of ~627 W/(m·K). The produced rGO/CNT composite film as a TIM will significantly improve the heat dissipation capability and has potential applications in thermal management of electronics.

Keywords: thermal interface materials; reduced graphene oxide; carbon nanotube; composite film

check for updates

Citation: Jiang, Y.; Song, S.; Mi, M.; Yu, L.; Xu, L.; Jiang, P.; Wang, Y. Improved Electrical and Thermal Conductivities of Graphene–Carbon Nanotube Composite Film as an Advanced Thermal Interface Material. *Energies* **2023**, *16*, 1378. https://doi.org/10.3390/en16031378

Academic Editors: Emigdio Chávez-Ángel and Jérémie Maire

Received: 30 December 2022
Revised: 27 January 2023
Accepted: 27 January 2023
Published: 30 January 2023

1. Introduction

With the development of portable devices and high−power electronics, more and more transistors are integrated per unit area, which produces a large amount of heat and causes severe heat dissipation issues. The rapid heat accumulation not only degrades the performance of electronic devices, but also affects the reliability and lifetime of electronic devices [1–3]. Therefore, effective thermal management is vital. A heat sink as a passive heat exchanger is attached to electronic devices to dissipate heat generated by the electronic devices. A vapor chamber, a two−phase heat spreading device, has been widely used for high heat flux applications [4,5], which is often integrated into the heat sink base and provides a maximum heat flux of 750 W/cm^2 [6]. However, due to uneven surfaces of the electronic devices and vapor chamber, air gaps with substantially low thermal conductivity (0.023 W/(m·K)) are formed therebetween [7], which create large thermal barriers to the heat dissipation path. Therefore, thermal interface materials (TIMs) are often required to fill the air gaps, to minimize the thermal contact resistance between the electronic devices and heat sink, and, thus, to ensure efficient heat dissipation. In addition to high thermal conductivity, TIMs must also have excellent flexibility to conform to surfaces [8].

The common traditional TIMs include thermally conductive grease, thermal pads, phase change materials, and thermal gel. However, most TIMs' thermal conductivity is less than 5 W/(m·K) [9,10], which cannot meet the urgent demands of highly integrated electronic devices and high−power electronics. Therefore, searching for novel materials with intrinsically high thermal conductivity as TIMs with enhanced characteristics is essential.

Since its discovery in 2004, graphene has attracted great attention and has been extensively studied in various fields. Graphene is reported to have a thermal conductivity as high as 3500–5300 W/(m·K) [11–13], which makes it one of the highest thermally conductive materials. Due to its exceptional thermal conductivity, graphene is considered as a promising next−generation thermal management material [14], and graphene−related materials have been widely used as TIMs and heat spreaders [15]. The top−down mechanical exfoliation method makes graphene with the highest quality, yet its meager yield limits its wide application in the industry [16]. The bottom−up chemical vapor deposition (CVD) method can make large−area graphene, yet the high price of produced graphene also hinders its inclusion in the industry [17]. Recently, the cost−effective and high−yield modified Hummers' method [18] has been developed to produce graphene, which pushes graphene toward industrial production for real−world applications. The Hummers' method first produces graphene oxide (GO) as a precursor of graphene through a chemical process. GO can self−assemble into macroscopic films by vacuum filtration, coating, and blade−casting methods, and the resulted GO film can be transformed into reduced graphene oxide (rGO) film by chemical (hydroiodic acid (HI) reduction) or thermal (carbonization and graphitization) reductions [19–21]. After carbonization at high temperature, oxygen functional groups are mostly removed, the lattice defects are repaired, and the sp^2 graphite crystal structure is restored. Therefore, the rGO is similar, in terms of structure and electronic properties, to pristine graphene [22].

Thermal conductivity is strongly related to the crystalline domain size and the concentration and type of defects [23,24]. The thermal conductivity of graphene is mainly contributed by phonons, and the repair of lattice defects by high−temperature treatment reduces phonon scattering centers and significantly improves the thermal conductivity of graphene. Therefore, the thermally reduced macroscopic rGO film has a high in−plane thermal conductivity exceeding 1500 W/(m·K) [25,26], which is much higher than that of copper (390 W/(m·K)), as the most commonly used heat spreader, showing the great application potentials of rGO film in thermal management as TIMs and heat spreaders.

However, due to the weak van der Waals (vdW) force between layers, rGO sheets tend to slide against each other, which leads to poor mechanical properties of rGO films. Moreover, although the rGO film has excellent in−plane thermal conductivity, the through−plane phonon transport is subject to severe scattering due to weak vdW interlayer interaction, such that its through−plane thermal conductivity is two orders of magnitude smaller than its in−plane thermal conductivity [27]. To improve the through−plane thermal conductivity and mechanical properties of rGO film, nanofillers, such as carbon polymer, carbon nanotube (CNT) [28], and metallic nanoparticles [29], etc., have been introduced to reinforce interlayer interactions of rGO sheets [30,31]. CNT has high thermal conductivity, high electrical conductivity, and outstanding mechanical properties, and, thus, are often used as thermally conductive fillers [32].

In this work, we systemically investigated the electrical, thermal, and mechanical properties of rGO/CNT composite films with various CNT concentrations. The composite films were fabricated by the vacuum−assistant filtration method. They were thermally reduced by Joule heating at >2000 K. Joule heating has been demonstrated to be a cost−effective and efficient method of fabricating high−quality rGO films [33]. During high−temperature carbonization, C–C covalent bonds are formed between graphene sheets and CNTs, and the added CNTs form a connection network between the adjacent graphene sheets. Compared with pure rGO film, the rGO/CNT composite film with an initial GO/CNT mass ratio of 4:1 exhibits significantly improved electrical and thermal conductivities. For example, electrical conductivity increases from ~1100 S/cm for the pure rGO film to ~2800 S/cm for the rGO/CNT(4:1) composite film, both reduced at 2400 K. Although the in−plane thermal conductivity decreases from ~918 W/(m·K) for the pure rGO film to ~627 W/(m·K) for the rGO/CNT(4:1) composite film, both reduced at 1000 K, the through−plane thermal conductivity of the composite film is improved. Further, the tensile strength increases from ~37 MPa for the pure GO film to ~80 MPa for the GO/CNT(4:1) composite film; the improved mechanical performance is due to the enhanced surface interaction.

2. Experiments

Materials: graphene oxide (GO) dispersion produced by improved Hummers' method and multi−walled carbon nanotubes (MWCNTs, purity > 95 wt%, outside diameter of 8–15 nm, and length of 50 μm) were purchased from Suzhou Tanfeng Technology.

Thermal treatment: Joule heating was performed in a vacuum chamber to prevent oxidization of the films, and a direct current was applied to the film.

Characterization: The X-ray diffraction (XRD) patterns were collected by an XRD diffractometer (Rigaku SmartLab, Tokyo in Japan) with Cu Kα radiation, λ = 1.5418 Å. The SEM images were obtained by Nova NanoSEM 450 (FEI, Hillsboro, OR, United States). The X-ray photoelectron spectroscopy (XPS) data were obtained on a PHI−5000 VersaprobeII (Ulvac−Phi, Chigasaki, Kanagawa, Japan) system under Al Kα radiation (hν = 1486.6 eV). The XPS spectra were calibrated based on the C−C 1s binding energy (284.8 eV). Raman spectra were collected on an inVia confocal Raman microscope (Renishaw, Wotton-under-Edge, United Kingdom) system at an excitation wavelength of 532 nm. Electrical conductivity measurements were performed by the four−point probe method using Keithley 2400 to supply current and measure voltage. The mechanical strength test was performed by ESM303 at a low speed (0.5 mm/min).

Thermal conductivity measurement: In−plane thermal conductivity was determined through thermal diffusivity according to $k = \alpha \times C_P \times \rho$, where k, α, C_P, and ρ represent thermal conductivity, thermal diffusivity, specific heat, and density, respectively. The thermal diffusivity was measured by a laser flash method, which is a well−developed method that conforms to many standards such as ISO 22007−4: 2008 and ASTM E1461. Specifically, a flash system (DLF−1200, TA Instruments, New Castle, DE, United States) uses an Nd:glass pulsed laser with a pulse width of 0.3 ms as the heating source to heat one side of the sample and a liquid nitrogen−cooled IR detector to measure the transient temperature response on the other side of the sample. The sample, which has been fabricated as a disk shape with a diameter of 25.4 mm and a thickness of ~5 μm, is placed in a sample holder for measurement. Specially designed masks are used to force in−plane heat transport in the sample film. Best−fitting the transient temperature signals as a function of time after the pulse heating yields the in−plane thermal diffusivity of the film, with a typical accuracy of ±3% as specified by the vendor. The specific heat capacities of the films were measured using the differential scanning calorimetry (DSC 2500 of TA Instrument), and the densities of the films were determined as the weight divided by the volume.

3. Results and Discussion

Figure 1 illustrates the preparation procedure of the thermally reduced rGO/CNT composite film. The evenly dispersed GO solution (2 mg/mL) and CNT aqueous solution (2 mg/mL) were mixed, and then a sonication treatment was performed to obtain a uniform mixture solution. To prepare GO/CNT composite films with various CNT concentrations, mass ratios of GO and CNTs in the mixture were 4:1, 2:1, 1:1, 1:2, and 1:4. Next, the GO/CNT composite films were prepared via the vacuum−assistant filtration method from the mixture solution, and the thickness of the composite film could be easily controlled by the amount of the mixture solution. The prepared freestanding GO/CNT composite films were reduced by thermal treatment, which includes two steps. First, the composite films were reduced at 1000 K for 5 h in an argon−hydrogen−filled furnace with a substantially low heating rate of 0.5 °C/min to obtain pre−reduced composite films. The low heating rate facilitates a slow escape rate of gases generated due to the decomposition of oxygen functional groups, which is important for the quality of the composite films. Second, the pre−reduced composite films were further thermally reduced in a high vacuum environment at a temperature ≥2000 K for 1 min by Joule heating. The high−temperature graphitization removes the remaining oxygen functional groups and repairs the defects of the graphite structure to increase the crystalline degree of the prepared rGO/CNT composite film. Finally, the rGO/CNT composite films were compressed to eliminate interlayer bubbles caused by gas release and obtain compact films.

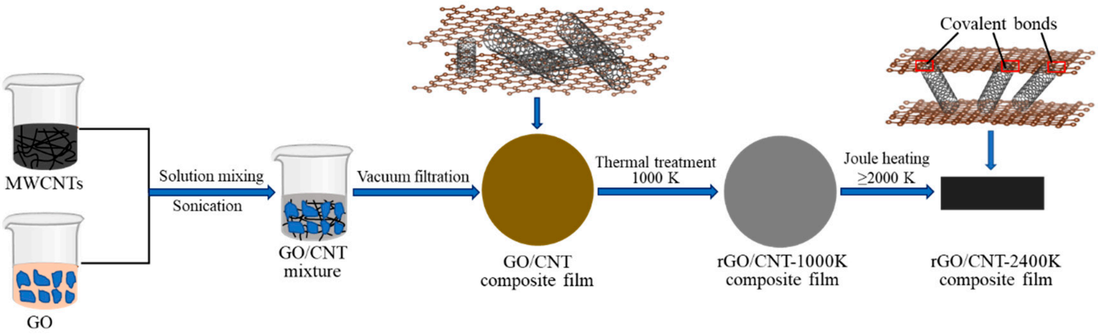

Figure 1. Preparation procedure of the thermally reduced rGO/CNT composite films.

Figure 2 shows the top view and cross−sectional view scanning electron microscope (SEM) images of the thermally reduced pure rGO film and the rGO/CNT composite film. For pure rGO film, the rGO sheets lie flat on top of each other and form a densely packed layer−by−layer structure. For the rGO/CNT composite film, the CNTs are uniformly embedded between rGO sheets and bridge the adjacent rGO sheets, thus providing additional interaction between rGO sheets to improve the mechanical strength and through−plane thermal conductivity of the composite film. The rGO/CNT composite films with various CNT concentrations have a similar structure, while CNTs might agglomerate at higher concentrations, as shown in Figure S1 in Supporting Information.

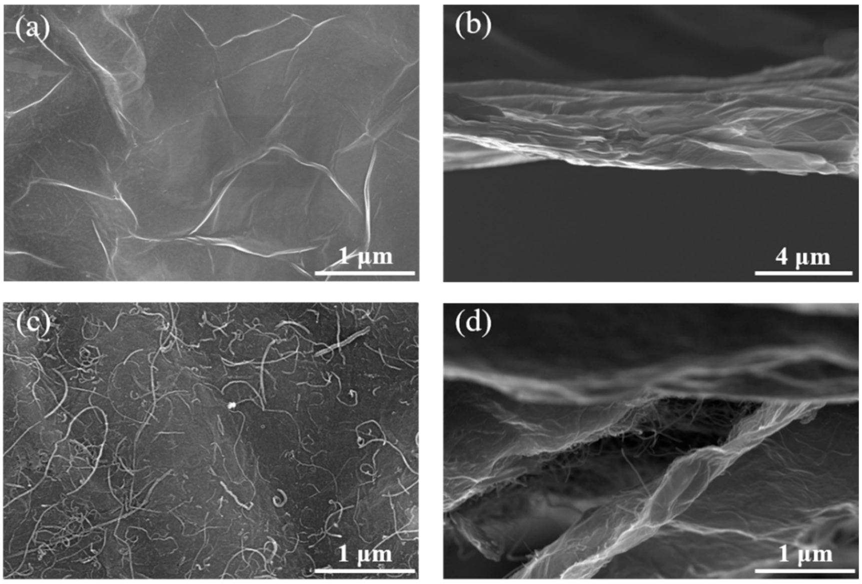

Figure 2. (**a**) Top view SEM image of rGO−1000 K film. (**b**) Cross−sectional view SEM image of rGO−2400 K film. (**c**,**d**) Top view (**c**) and cross−sectional view (**d**) SEM images of rGO/CNT(4:1)−1000 K composite film.

The structure, defects, and composition features of the rGO/CNT composite films and their evolution as a function of reduction temperature were further characterized by Raman spectroscopy, X-ray diffraction (XRD) analyses, and X-ray photoelectron spectroscopy (XPS). Figure 3a illustrates the XRD patterns of GO and rGO films. The diffraction peak becomes sharp and narrow as the reduction temperature increases, which indicates that the interlayer distance gradually decreases and the crystalline grain size gradually increases as the reduction temperature increases. Similar phenomena were also observed for rGO/CNT composite films, as shown in Figure 3b. The extracted interlayer distance for GO film was 0.8975 nm, which is ascribed to the presence of oxygen functional groups that separate the graphene sheets. Thermal reduction at high temperatures gradually removes the oxygen functional groups and thus decreases interlayer distance, e.g., 0.3436 nm for rGO film reduced at 2400 K. The through−plane crystalline grain size (L_c) can be extracted from the XRD pattern according to the Scherrer equation $L_c = \frac{\kappa\lambda}{\beta cos\theta}$ [34,35], where κ equals 0.89 and β is full width at half maximum. The L_c of the GO film is 0.1669 nm, while the L_c of rGO film first decreases to 0.0797 nm after being reduced at 1000 K and then increases to 0.4177 nm after being reduced at 2400 K. The decrease of L_c for 1000 K−reduced rGO film is ascribed to the formation of defects such as vacancies and distortions caused by the removal of oxygen functional groups [36], and the increase of L_c for 2400 K−reduced rGO film is ascribed to the high−temperature carbonization for repairing the structural defects. The evolution of interlayer distance and crystalline grain size as a function of reduction temperature for rGO/CNT composite films is similar to that of the rGO films, as shown in Figure S2 in Supporting Information. Further, the XRD pattern of the pure CNT film is also similar to that of the rGO film (Figure S3 in Supporting Information), confirming that the change of the peak is due to the decrease of interlayer distance. Table 1 lists the interlayer distance and L_c for rGO films and rGO/CNT composite films reduced at different temperatures.

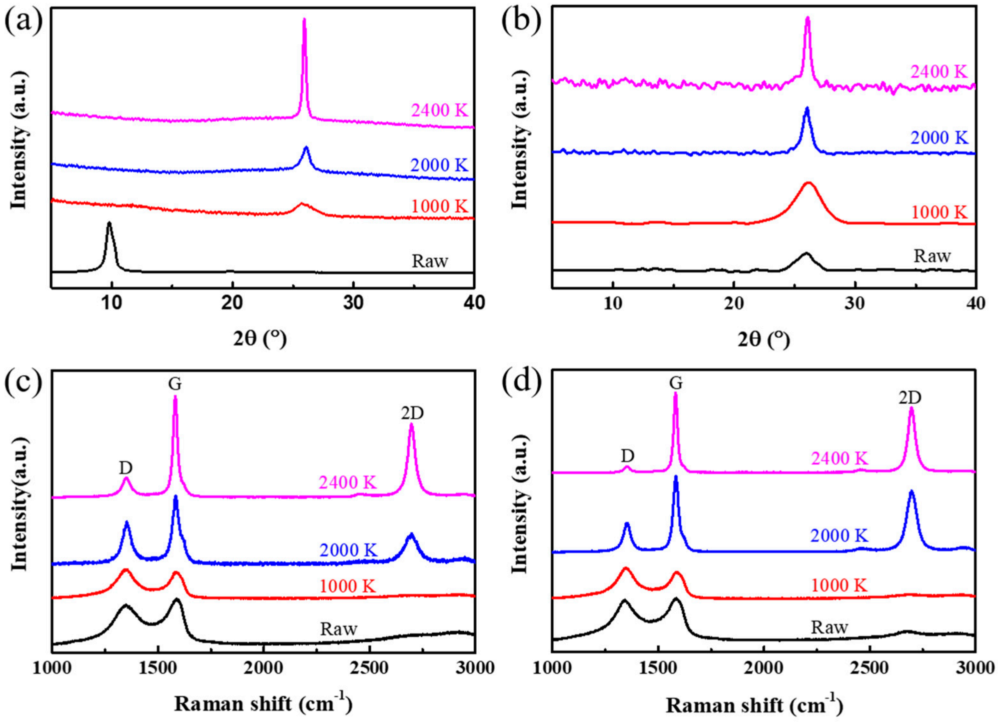

Figure 3. (**a**,**b**) XRD patterns of the rGO films (**a**) and rGO/CNT(4:1) composite films (**b**) reduced at various temperatures. (**c**,**d**) Raman spectra of the rGO films (**c**) and rGO/CNT(4:1) composite films (**d**) reduced at various temperatures.

Table 1. Structural parameters of the rGO films and rGO/CNT(4:1) composite films.

Samples	**GO**	**rGO−1000 K**	**rGO−2400 K**	**GO/CNT(4:1)**	**rGO/CNT(4:1)−1000 K**	**rGO/CNT(4:1)−2400 K**
d/nm	0.8975	0.3446	0.3436	0.3437	0.3432	0.3422
L_c/nm	0.1669	0.0797	0.4177	0.0730	0.0578	0.2653
I_D/I_G	0.84	1.16	0.13	0.96	1.14	0.08
L_a/nm	22.89	16.57	147.88	20.02	16.86	240.30

Raman spectroscopy was used to characterize the structural fingerprint, such as the disorder and defects of the material. As shown in Figure 3c, the GO film displays two peaks at 1350 cm^{-1} and 1580 cm^{-1}, which correspond to the D band and G band of graphene, respectively. The D band represents the breathing mode of sp^2 carbon rings adjacent to a defect or an edge, and the G band arises from the in−plane stretching mode of sp^2 carbon atoms [37]. The ratio of the intensity of the D band over the intensity of the G band (I_D/I_G ratio) is often used to recognize the density of defects in graphene [38]. For example, if the GO film is reduced at 1000 K, the I_D/I_G ratio increases from 0.84 to 1.16, suggesting increased defect density. After the GO film is reduced at 2400 K, the D band almost disappears, and the I_D/I_G ratio decreases to 0.13, indicating effective removal of oxygen functional groups and the repair of defects after high−temperature graphitization [39]. Further, after the GO film is reduced at a temperature greater than 2000 K, in addition to the D and G bands, the 2D peak at 2700 cm^{-1} appears, which reflects the high crystalline structure of the rGO film reduced at higher temperature [40,41]. For the Raman spectra of the rGO/CNT composite films, similar features and evolution as a function of the reduction temperature were observed, as shown in Figure 3d and Figure S4 in Supporting Information. Further, the in−plane crystalline size (L_a) can be extracted from the Raman spectra according to Cancado's formula $L_a = \left(2.4 \times 10^{-10}\right)\lambda^4 (I_D/I_G)^{-1}$ [42], as shown in Table 1. The XRD and Raman results demonstrate that the in−plane and through−plane crystalline size of both the rGO films and the rGO/CNT composite films first decrease after being reduced at 1000 K, and then significantly increase after being reduced at 2400 K, indicating a high crystalline structure of the high−temperature−reduced rGO film and the rGO/CNT composite film.

XPS was used to characterize the composition of the rGO films and the rGO/CNT composite films, which reveals the evolution of the atomic concentration of carbon as a function of the reduction temperature. As shown in Figure 4a, the C/O atomic ratio significantly increases from 2.16 of the GO/CNT(4:1) composite film to 12.97 of the 2400 K−reduced rGO/CNT(4:1) composite film, indicating the effective removal of the oxygen functional groups. Moreover, as shown in Figure 4b–d, the high−resolution C1s XPS spectra were fitted with a set of components (e.g., C=C, C−O−C, and O−C=O, etc.) to quantify the content of sp^2 carbon atoms. Results show that after the composite film is reduced at high temperatures, the content of C=C bonds dramatically increases from 52.67% to 82.16 %, indicating the significantly improved crystalline quality of the 2400 K−reduced rGO/CNT composite film.

The electrical conductivities of the rGO films and the rGO/CNT composite films with various CNT concentrations as a function of the reduction temperature were measured by a four−point probe method, as shown in Figure 5a. Figure 5b shows the electrical conductivities of both the rGO films and the rGO/CNT composite films. The raw GO film is insulating, and the addition of CNTs improves the electrical conductivity of GO/CNT composite film due to the hopping of electrons. The electrical conductivity of GO/CNT composite film increases as the concentration of CNTs increases, as shown in Figure S5 in Supporting Information, and reaches ~0.2 S/cm for GO/CNT(1:4) composite film. As the reduction temperature increases, the electrical conductivity of the film increases. Moreover, after adding a small amount of CNTs, the electrical conductivity increases. For example, the electrical conductivity increases from ~1105 S/cm for the pure rGO film to ~2827 S/cm for the rGO/CNT(4:1) composite film, both reduced at 2400 K. The improved electrical conductivity for the rGO/CNT(4:1) composite film is due to the formation of C–C covalent bonds between rGO sheets and CNTs and the connection between rGO sheets by CNTs. As the concentration of CNTs increases, the electrical conductivity of the rGO/CNT composite film decreases due to the agglomeration of CNTs. The rGO/CNT(4:1)−2400 K film exhibits the desired electrical conductivity.

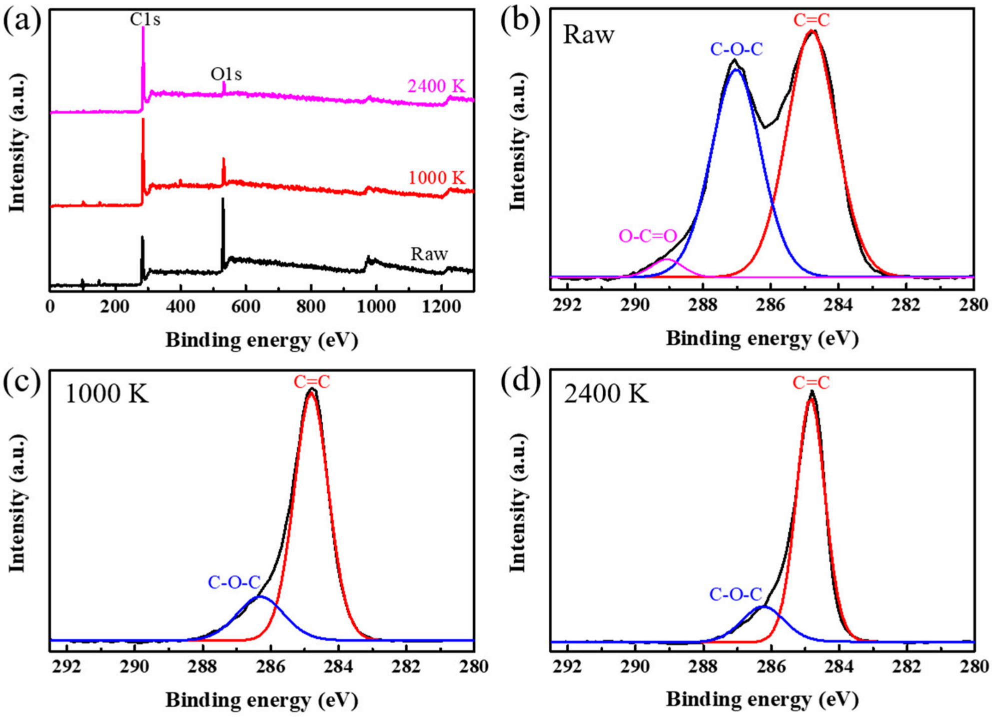

Figure 4. (**a**) High−resolution XPS spectra of the GO/CNT(4:1), rGO/CNT(4:1)−1000 K, and rGO/CNT(4:1)−2400 K films. (**b–d**) C1s XPS spectra of GO/CNT(4:1) (**b**), rGO/CNT(4:1)−1000 K (**c**), and rGO/CNT(4:1)−2400 K (**d**) films.

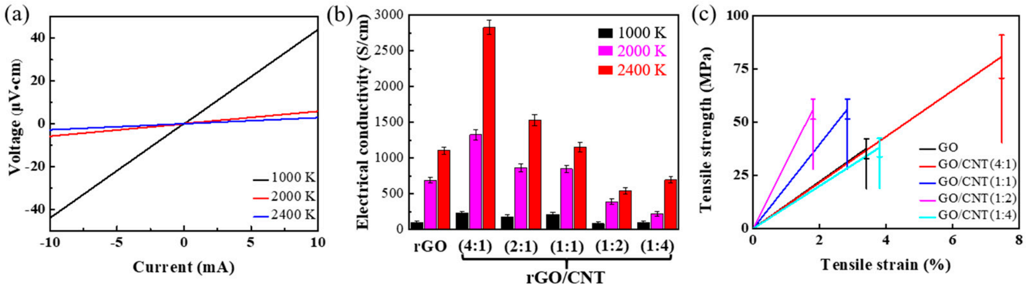

Figure 5. (**a**) I–V curves of the four−point probe measurement of the rGO/CNT(4:1) composite films reduced at 1000 K, 2000 K, and 2400 K. (**b**) Electrical conductivities of the rGO films and the rGO/CNT composite films with various CNT concentrations reduced at 1000 K, 2000 K, and 2400 K. (**c**) Tensile strength of GO, GO/CNT(4:1), GO/CNT(1:1), GO/CNT(1:2), and GO/CNT(1:4) films.

The initial mechanical strength of the composite films with various CNT concentrations was further tested, with the results shown in Figure 5c. The addition of appropriate amounts of CNTs significantly improves the tensile strength of the film, which is due to the increase of the interlayer interaction and the reduced interlayer slipping between graphene sheets. For example, the tensile strength increases from ~37 MPa for GO film to ~80 MPa for the GO/CNT(4:1) composite film. The tensile strength does not increase monotonically with the CNT concentration, which is probably due to the agglomeration of CNTs at higher concentrations.

We further investigate the thermal conductivities of the rGO film and the rGO/CNT composite films. The in−plane thermal diffusivities of the films are measured using the laser flash method, a schematic of which is shown in Figure 6a. Figure 6b shows the in−plane thermal conductivities of the rGO film and the rGO/CNT composite films, all reduced at 1000 K. The in−plane thermal conductivity of the film decreases after adding CNTs, and the reduction is more significant as the concentration of CNTs increases. For example, the in−plane thermal conductivity decreases from 918 ± 44 W/(m·K) for the rGO film to 627 ± 34 W/(m·K), 573 ± 30 W/(m·K), 552 ± 31 W/(m·K), and 497 ± 33 W/(m·K) for the rGO/CNT(4:1), rGO/CNT(2:1), rGO/CNT(1:1), and rGO/CNT(1:2) composite films, respectively. The decrease of in−plane thermal conductivity of the rGO/CNT composite film is probably due to the increased in−plane separation between graphene sheets by CNTs.

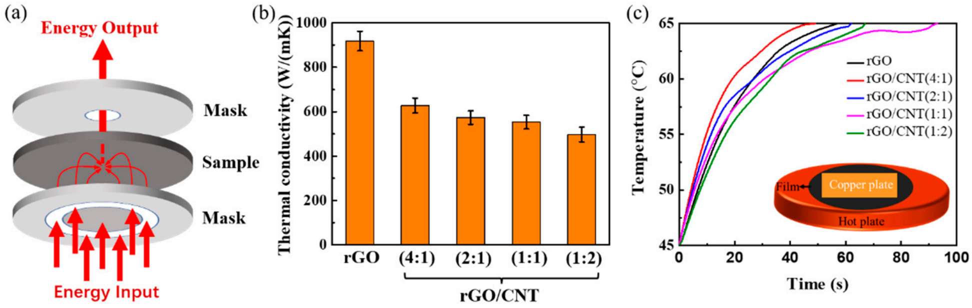

Figure 6. (**a**) Schematic diagram of the laser flash method for measuring in−plane thermal diffusivities of the films. (**b**) In−plane thermal conductivities of the rGO film and the rGO/CNT composite films with various CNT concentrations, all reduced at 1000 K. (**c**) Time required for the copper plate to rise from 45 °C to 65 °C with the rGO film and the rGO/CNT composite films, all reduced at 1000 K, as TIMs. The insert shows a schematic of the setup.

On the other hand, the films' through−plane thermal conductivities are hard to measure using the laser flash method due to the films' very small thickness; neither can they be measured by the thermo−reflectance techniques due to the surface roughness. Here, we use the rGO film and the rGO/CNT composite films as TIMs between a copper plate and a hot plate, as shown in the inset in Figure 6c. The hot plate's temperature is kept at 80 °C. After the copper plate and the TIM film are placed on the hot plate, an infrared camera (Guide D384M) records the temperature of the copper plate in real time, with the results shown in Figure 6c. Among all the films, the rGO/CNT(4:1) composite film requires the shortest time (49 s) to be heated up from 45 °C to 65 °C, indicating that the rGO/CNT(4:1) composite film has higher through−plane thermal conductivity than the other films. The results suggest that adding an appropriate amount of CNTs increases the interlayer interaction of graphene sheets and improves the through−plane thermal conductivity of the film. Although the in−plane thermal conductivity of the rGO/CNT(4:1) composite film slightly decreases compared to the rGO film, the through−plane thermal conductivity increases, which is more advantageous for the application of rGO/CNT composite films as TIMs because the heat transfer from the chip to the heat sink is often along the through−plane direction [43].

4. Conclusions

In summary, we successfully fabricated rGO/CNT composite films with desired electrical and thermal conductivities. Further, the effect of CNT concentrations on the properties of the composite films was systematically investigated. At a small CNT concentration, the added CNTs connect the graphene sheets and increase the interlayer interaction, thereby significantly improving the composite film's electrical and through−plane thermal properties compared to the pure rGO film. At a high CNT concentration, due to the agglomeration of CNTs, the properties of the composite film degrade. Among the investigated composite films, the rGO/CNT(4:1) film has the best performance: electrical conductivity of ~2827 S/cm after being reduced at 2400 K and in−plane thermal conductivity of ~627 W/(m·K) after being reduced at 1000 K. Our results will be helpful for further optimizing carbon−based TIMs, especially for improving the through−plane thermal conductivity of TIMs. TIMs with high through−plane thermal conductivity will significantly improve the heat dissipation capacity of electronic devices, which facilitates a high integration degree and high power. Next, the through−plane thermal conductivity of the rGO/CNT composite film needs to be quantitatively determined, and the fabrication method of the rGO/CNT composite film needs to be optimized to make large−scale films with various thickness, which are required in the industry.

Supplementary Materials: The following supporting information can be downloaded at: https://www.mdpi.com/article/10.3390/en16031378/s1, Figure S1: SEM image of rGO/CNT(1:4)−1000 K composite film, showing the agglomeration of CNTs at higher concentration; Figure S2: XRD patterns of rGO/CNT(2:1) film (a), rGO/CNT(1:1) film (b), rGO/CNT(1:2) film (c), and rGO/CNT(1:4) film (d) reduced at different temperatures; Figure S3: XRD patterns of rGO film and CNT film, both reduced at 1000 K; Figure S4: Raman spectra of rGO/CNT(2:1) film (a), rGO/CNT(1:1) film (b), rGO/CNT(1:2) film (c), and rGO/CNT(1:4) film (d) reduced at different temperatures; Figure S5: I−V curves of the measurement of the raw GO/CNT composite films. The electrical conductivities of the GO/CNT(4:1), GO/CNT(2:1), GO/CNT(1:1), GO/CNT(1:2) and GO/CNT(1:4) composite films are 1.2×10^{-6} S/cm, 4.8×10^{-3} S/cm, 2.6×10^{-2} S/cm, 0.14 S/cm, and 0.2 S/cm, respectively.

Author Contributions: Y.W. conceived the project. Y.J. prepared the films. Y.J. and M.M. performed XRD, XPS, and Raman measurements. Y.J. and L.Y. performed electrical conductivity measurement. L.Y. and L.X. performed SEM measurements. S.S. performed in−plane thermal conductivity measurements under the supervision of P.J. Y.J., L.X. and Y.W. wrote the manuscript and all authors participated in discussing the results and revising the manuscript. All authors have read and agreed to the published version of the manuscript.

Funding: This work was supported by the Qilu Young Scholar Program of Shandong University.

Data Availability Statement: Data is contained within the article or supplementary material.

Conflicts of Interest: The authors declare no conflict of interest.

References

1. Chen, H.; Ginzburg, V.V.; Yang, J.; Yang, Y.; Liu, W.; Huang, Y.; Du, L.; Chen, B. Thermal conductivity of polymer-based composites: Fundamentals and applications. *Prog. Polym. Sci.* **2016**, *59*, 41–85. [CrossRef]
2. Khan, J.; Momin, S.A.; Mariatti, M. A review on advanced carbon-based thermal interface materials for electronic devices. *Carbon* **2020**, *168*, 65–112. [CrossRef]
3. Moore, A.L.; Shi, L. Emerging challenges and materials for thermal management of electronics. *Mater. Today* **2014**, *17*, 163–174. [CrossRef]
4. Bulut, M.; Kandlikar, S.G.; Sozbir, N. A Review of Vapor Chambers. *Heat Transf. Eng.* **2019**, *40*, 1551–1573. [CrossRef]
5. Velardo, J.; Singh, R.; Date, A.; Date, A. An investigation into the effective thermal conductivity of vapour chamber heat spreaders. *Energy Procedia* **2017**, *110*, 256–261. [CrossRef]
6. Górecki, K.; Posobkiewicz, K. Cooling Systems of Power Semiconductor Devices—A Review. *Energies* **2022**, *15*, 4566. [CrossRef]
7. Wu, X.; Wang, H.; Wang, Z.; Xu, J.; Wu, Y.; Xue, R.; Cui, H.; Tian, C.; Wang, Y.; Huang, X.; et al. Highly conductive thermal interface materials with vertically aligned graphite-nanoplatelet filler towards: High power density electronic device cooling. *Carbon* **2021**, *182*, 445–453. [CrossRef]
8. Due, J.; Robinson, A.J. Reliability of thermal interface materials: A review. *Appl. Therm. Eng.* **2013**, *50*, 455–463. [CrossRef]
9. Gao, J.; Yan, Q.; Lv, L.; Tan, X.; Ying, J.; Yang, K.; Yu, J.; Du, S.; Wei, Q.; Xiang, R.; et al. Lightweight thermal interface materials based on hierarchically structured graphene paper with superior through-plane thermal conductivity. *Chem. Eng. J.* **2021**, *419*, 129609. [CrossRef]
10. Shahil, K.M.F.; Balandin, A.A. Graphene–Multilayer Graphene Nanocomposites as Highly Efficient Thermal Interface Materials. *Nano Lett.* **2012**, *12*, 861–867. [CrossRef]
11. Balandin, A.A.; Ghosh, S.; Bao, W.; Calizo, I.; Teweldebrhan, D.; Miao, F.; Lau, C.N. Superior Thermal Conductivity of Single-Layer Graphene. *Nano Lett.* **2008**, *8*, 902–907. [CrossRef]

12. Chen, S.; Moore, A.L.; Cai, W.; Suk, J.W.; An, J.; Mishra, C.; Amos, C.; Magnuson, C.W.; Kang, J.; Shi, L.; et al. Raman Measurements of Thermal Transport in Suspended Monolayer Graphene of Variable Sizes in Vacuum and Gaseous Environments. *ACS Nano* **2011**, *5*, 321–328. [CrossRef]
13. Chen, S.; Wu, Q.; Mishra, C.; Kang, J.; Zhang, H.; Cho, K.; Cai, W.; Balandin, A.A.; Ruoff, R.S. Thermal conductivity of isotopically modified graphene. *Nat. Mater.* **2012**, *11*, 203–207. [CrossRef]
14. Gong, F.; Li, H.; Wang, W.; Xia, D.; Liu, Q.; Papavassiliou, D.; Xu, Z. Recent Advances in Graphene-Based Free-Standing Films for Thermal Management: Synthesis, Properties, and Applications. *Coatings* **2018**, *8*, 63. [CrossRef]
15. Fu, Y.; Hansson, J.; Liu, Y.; Chen, S.; Zehri, A.; Samani, M.K.; Wang, N.; Ni, Y.; Zhang, Y.; Zhang, Z.-B.; et al. Graphene related materials for thermal management. *2D Mater.* **2020**, *7*, 012001. [CrossRef]
16. Van Noorden, R. Moving towards a graphene world. *Nature* **2006**, *442*, 228–229. [CrossRef]
17. Zhang, Y.; Zhang, L.; Zhou, C. Review of Chemical Vapor Deposition of Graphene and Related Applications. *Acc. Chem. Res.* **2013**, *46*, 2329–2339. [CrossRef]
18. Marcano, D.C.; Kosynkin, D.V.; Berlin, J.M.; Sinitskii, A.; Sun, Z.; Slesarev, A.; Alemany, L.B.; Lu, W.; Tour, J.M. Improved synthesis of graphene oxide. *ACS Nano* **2010**, *4*, 4806–4814. [CrossRef]
19. Peng, L.; Xu, Z.; Liu, Z.; Guo, Y.; Li, P.; Gao, C. Ultrahigh Thermal Conductive yet Superflexible Graphene Films. *Adv. Mater.* **2017**, *29*, 1700589. [CrossRef]
20. Kumar, P.; Shahzad, F.; Yu, S.; Hong, S.M.; Kim, Y.-H.; Koo, C.M. Large-area reduced graphene oxide thin film with excellent thermal conductivity and electromagnetic interference shielding effectiveness. *Carbon* **2015**, *94*, 494–500. [CrossRef]
21. Jin, S.; Gao, Q.; Zeng, X.; Zhang, R.; Liu, K.; Shao, X.; Jin, M. Effects of reduction methods on the structure and thermal conductivity of free-standing reduced graphene oxide films. *Diam. Relat. Mater.* **2015**, *58*, 54–61. [CrossRef]
22. Gómez-Navarro, C.; Meyer, J.C.; Sundaram, R.S.; Chuvilin, A.; Kurasch, S.; Burghard, M.; Kern, K.; Kaiser, U. Atomic structure of reduced graphene oxide. *Nano Lett.* **2010**, *10*, 1144–1148. [CrossRef]
23. Maldovan, M. Sound and heat revolutions in phononics. *Nature* **2013**, *503*, 209–217. [CrossRef]
24. Parrott, J.E.; Stuckes, A.D.; Klemens, P.G. Thermal Conductivity of Solids. *Phys. Today* **1977**, *30*, 60–61. [CrossRef]
25. Akbari, A.; Cunning, B.V.; Joshi, S.R.; Wang, C.; Camacho-Mojica, D.C.; Chatterjee, S.; Modepalli, V.; Cahoon, C.; Bielawski, C.W.; Bakharev, P.; et al. Highly Ordered and Dense Thermally Conductive Graphitic Films from a Graphene Oxide/Reduced Graphene Oxide Mixture. *Matter* **2020**, *2*, 1198–1206. [CrossRef]
26. Zhang, Y.; Han, H.; Wang, N.; Zhang, P.; Fu, Y.; Murugesan, M.; Edwards, M.; Jeppson, K.; Volz, S.; Liu, J. Improved heat spreading performance of functionalized graphene in microelectronic device application. *Adv. Funct. Mater.* **2015**, *25*, 4430–4435. [CrossRef]
27. Renteria, J.D.; Ramirez, S.; Malekpour, H.; Alonso, B.; Centeno, A.; Zurutuza, A.; Cocemasov, A.I.; Nika, D.L.; Balandin, A.A. Strongly Anisotropic Thermal Conductivity of Free-Standing Reduced Graphene Oxide Films Annealed at High Temperature. *Adv. Funct. Mater.* **2015**, *25*, 4664–4672. [CrossRef]
28. Jia, H.; Kong, Q.-Q.; Liu, Z.; Wei, X.-X.; Li, X.-M.; Chen, J.-P.; Li, F.; Yang, X.; Sun, G.-H.; Chen, C.-M. 3D graphene/ carbon nanotubes/ polydimethylsiloxane composites as high-performance electromagnetic shielding material in X-band. *Compos. Part A Appl. Sci. Manufac.* **2020**, *129*, 105712. [CrossRef]
29. Chen, Y.; Hou, X.; Liao, M.; Dai, W.; Wang, Z.; Yan, C.; Li, H.; Lin, C.-T.; Jiang, N.; Yu, J. Constructing a “pea-pod-like” alumina-graphene binary architecture for enhancing thermal conductivity of epoxy composite. *Chem. Eng. J.* **2020**, *381*, 122690. [CrossRef]
30. Pan, T.-W.; Kuo, W.-S.; Tai, N.-H. Tailoring anisotropic thermal properties of reduced graphene oxide/multi-walled carbon nanotube hybrid composite films. *Compos. Sci. Technol.* **2017**, *151*, 44–51. [CrossRef]
31. Yuan, H.-C.; Lee, C.-Y.; Tai, N.-H. Extremely high thermal conductivity of nanodiamond-polydopamine/thin-layer graphene composite films. *Compos. Sci. Technol.* **2018**, *167*, 313–322. [CrossRef]
32. Rathinavel, S.; Priyadharshini, K.; Panda, D. A review on carbon nanotube: An overview of synthesis, properties, functionalization, characterization, and the application. *Mater. Sci. Eng. B* **2021**, *268*, 115095. [CrossRef]
33. Wang, Y.; Chen, Y.; Lacey, S.D.; Xu, L.; Xie, H.; Li, T.; Danner, V.A.; Hu, L. Reduced graphene oxide film with record-high conductivity and mobility. *Mater. Today* **2018**, *21*, 186–192. [CrossRef]
34. Langford, J.I.; Wilson, A.J.C. Scherrer after sixty years: A survey and some new results in the determination of crystallite size. *J. Appl. Crystallogr.* **1978**, *11*, 102–113. [CrossRef]
35. Monshi, A.; Foroughi, M.R.; Monshi, M.R. Modified Scherrer Equation to Estimate More Accurately Nano-Crystallite Size Using XRD. *World J. Nano Sci. Eng.* **2012**, *02*, 154–160. [CrossRef]
36. Chen, C.-M.; Huang, J.-Q.; Zhang, Q.; Gong, W.-Z.; Yang, Q.-H.; Wang, M.-Z.; Yang, Y.-G. Annealing a graphene oxide film to produce a free standing high conductive graphene film. *Carbon* **2012**, *50*, 659–667. [CrossRef]
37. Yang, D.; Velamakanni, A.; Bozoklu, G.; Park, S.; Stoller, M.; Piner, R.D.; Stankovich, S.; Jung, I.; Field, D.A.; Ventrice, C.A.; et al. Chemical analysis of graphene oxide films after heat and chemical treatments by X-ray photoelectron and Micro-Raman spectroscopy. *Carbon* **2009**, *47*, 145–152. [CrossRef]
38. Shen, Y.; Zhang, H.-B.; Zhang, H.; Ren, W.; Dasari, A.; Tang, G.-S.; Yu, Z.-Z. Structural evolution of functionalized graphene sheets during solvothermal reduction. *Carbon* **2013**, *56*, 132–138. [CrossRef]

39. Song, L.; Khoerunnisa, F.; Gao, W.; Dou, W.; Hayashi, T.; Kaneko, K.; Endo, M.; Ajayan, P.M. Effect of high-temperature thermal treatment on the structure and adsorption properties of reduced graphene oxide. *Carbon* **2013**, *52*, 608–612. [CrossRef]
40. Hu, C.; Sedghi, S.; Silvestre-Albero, A.; Andersson, G.G.; Sharma, A.; Pendleton, P.; Rodríguez-Reinoso, F.; Kaneko, K.; Biggs, M.J. Raman spectroscopy study of the transformation of the carbonaceous skeleton of a polymer-based nanoporous carbon along the thermal annealing pathway. *Carbon* **2015**, *85*, 147–158. [CrossRef]
41. Lu, H.; Zhang, J.; Luo, J.; Gong, W.; Li, C.; Li, Q.; Zhang, K.; Hu, M.; Yao, Y. Enhanced thermal conductivity of free-standing 3D hierarchical carbon nanotube-graphene hybrid paper. *Compos. Part A Appl. Sci. Manufac.* **2017**, *102*, 1–8. [CrossRef]
42. Cançado, L.G.; Takai, K.; Enoki, T.; Endo, M.; Kim, Y.A.; Mizusaki, H.; Jorio, A.; Coelho, L.N.; Magalhães-Paniago, R.; Pimenta, M.A. General equation for the determination of the crystallite size La of nanographite by Raman spectroscopy. *Appl. Phys. Lett.* **2006**, *88*, 163106. [CrossRef]
43. Xue, Y.; Li, X.; Wang, H.; Zhao, F.; Zhang, D.; Chen, Y. Improvement in thermal conductivity of through-plane aligned boron nitride/silicone rubber composites. *Mater Des.* **2019**, *165*, 107580. [CrossRef]